Fabry-Perot cavity-based circularly polarized Sierpinski fractal antenna with analysis and measurement characterization for sub 5/6G V2I and V2V communication

scientific reports

OPEN

Fabry–Perot cavity-based circularly polarized Sierpinski fractal antenna with analysis and measurement characterization for sub 5/6G V2I and V2V communication

Fatima Ez-zaki[1], Shahid Khan[2], Omar Ourahou[3], Hassan Belahrach[3,4], Abdelilah Ghammaz[3], Salahuddin Khan[5], Jamal Nasir[2], Slawomir Koziel[2,6], Sadiq Ullah[7] & Ladislau Matekovits[8,9,10]✉

This paper presents the design, fabrication, and performance analysis of a high-gain, broadband circularly polarized (CP) Fabry–Perot cavity (FPC) antenna tailored for vehicular communication applications. The proposed antenna employs a frequency-selective surface (FSS)-based partially reflective surface (PRS) superstrate, fabricated on Rogers 5880 substrate, to enhance gain and 3-dB gain bandwidth. At the core of the design is a Sierpinski fractal-shaped radiating element with corner etching, which effectively addresses the narrow axial ratio (AR) bandwidth limitations typically associated with circularly polarized (CP) antennas. The single-element configuration yields a gain of 3.8 dBc, which increases to 7 dBc in a two-element array arrangement. Integrating a Fabry–Perot configuration with a single PRS superstrate of 1.575 mm thickness and positioned 24.6 mm above the radiating patch further improves the performance, achieving 15.5 dBc gain and enhanced AR bandwidth centered around 5.9 GHz. To further augment the performance, a PRS with a positive phase gradient is introduced, resulting in a stable peak gain of 17.72 dBc and improved beam width and polarization stability. Comprehensive simulations and measurements show excellent agreement, validating the proposed antenna's suitability for high-performance, real-world vehicle-to-vehicle (V2V), vehicle-to-infrastructure (V2I), and vehicle-to-everything (V2X) communication systems.

Keywords FSS, CP, Fabry–Perot, Sierpinski fractal, PRS, Measurement, V2V, V2I

The rise in end-user mobility has led to a significant increase in traffic congestion, fatalities, and injuries. Prioritizing passenger safety and enhancing traffic flow to eliminate road traffic fatalities has become crucial. To tackle these issues, the V2X communications paradigm was introduced, aiming to reduce congestion and accidents, especially at toll plazas. When combined with advanced driver-assistance systems (ADAS) sensors, V2X, along with V2V, V2I, Vehicle-to-Pedestrian (V2P), and Vehicle-to-Network (V2N) communication, and Vehicle-to-Cloud (V2C), seeks to enhance safety, improve situational awareness, boost traffic efficiency, and ultimately optimize transportation systems[1].

[1]Laboratory of Innovation in Management and Engineering for Business (LIMIE), Higher Institute of Engineering and Business (ISGA), Marrakech, Morocco. [2]Department of Elecrical Engineering , COMSATS University Islamabad, Abbottabad Campus, 22044 Abbottabad, Pakistan. [3]LSEEET Laboratory, Faculty of Sciences and Technologies, Cadi Ayyad University, Av Abdelkrim Khattabi, Marrakech, Morocco. [4]Royal School of Aeronautics, 40160 Marrakesh, Morocco. [5]College of Engineering, King Saud University, P.O. Box 800, 11421 Riyadh, Saudi Arabia. [6]Engineering Optimization and Modeling Center, Reykjavik University, 101 Reykjavik, Iceland. [7]Electrical Engineering Department, Faculty of Engineering, University of Tabuk, 47913 Tabuk, Saudi Arabia. [8]Department of Electronics and Telecommunications, Politecnico Di Torino, 10129 Turin, Italy. [9]Department of Measurements and Optical Electronics, Politehnica University Timisoara, 300006 Timisoara, Romania. [10]Istituto Di Elettronica E Di Ingegneria dellInformazione E Delle Telecomunicazioni, National Research Council, 10129 Turin, Italy. ✉email: ladislau.matekovits@polito.it

V2X communication enables high-speed duplex data exchange between onboard units (OBU) in vehicles and roadside equipment (RSE) on road infrastructure, as illustrated in Fig. 1. This is achieved using Dedicated Short-Range Communication (DSRC) and Cellular V2X (C-V2X) standards[1]. In the United States, the 5.850–5.925 GHz frequency band is designated for DSRC, allowing communications over line-of-sight (LoS) ranges up to 1000 m under optimal weather conditions[2,3]. In Europe, the EN12253 standard outlines DSRC requirements at 5.8 GHz, including criteria for antenna performance[1]. Considering the varied range and data rate needs of V2X communications, the forthcoming 5G network integrates both millimeter-wave (mmWave) and sub-6 GHz bands to effectively handle the diverse scenarios in V2X applications.

Vehicular communication systems, including V2V and V2I, demand antenna solutions that combine high gain, broad bandwidth, and circular polarization to ensure robust performance in dynamic, interference-rich environments. Such characteristics are critical for enhancing signal strength, extending communication range, mitigating multipath fading, and ensuring reliable connectivity, especially as modern vehicles are now equipped with over 40 functional antennas[1]. However, many conventional antenna designs struggle with narrow AR bandwidth, low gain, or intricate multilayer geometries, limiting their scalability and practical integration into vehicles. To address the performance requirements of DSRC roadside equipment, researchers have explored a wide array of antenna configurations, including multilayered structures[2], sequentially rotated arrays[3,4], double-looped monopole arrays[4], Yagi dipole arrays[5], and CP array topologies[6]. Among these, CP antennas have proven especially effective in suppressing side lobe levels (SLL), thereby improving resistance to environmental degradation and enhancing reception of scattered or diffracted signals. Nevertheless, many

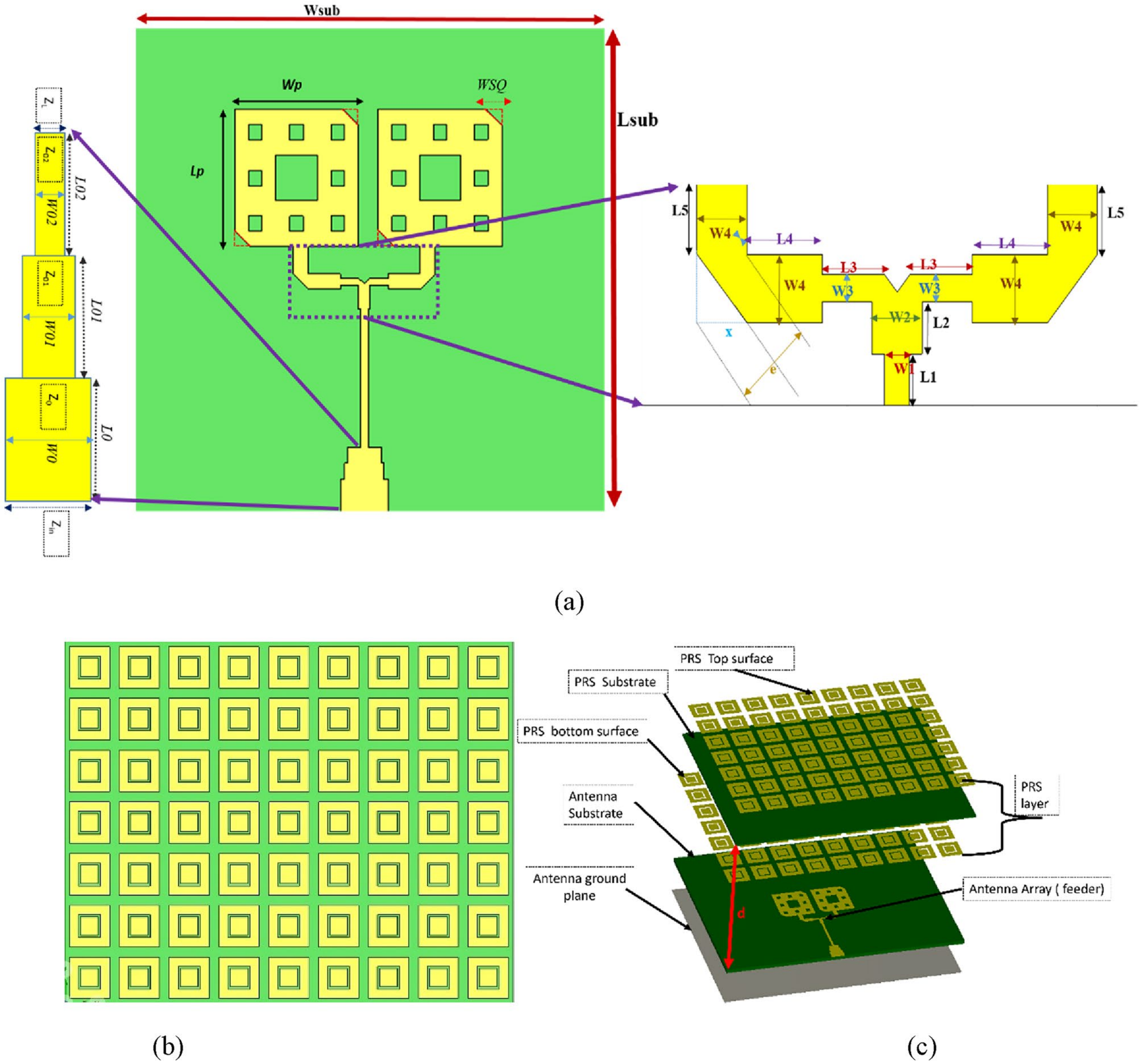

Fig. 1. Geometry of the proposed single-element antenna: (**a**) Front view, (**b**) side view, and (**c**) exploded view.

of these approaches still involve manufacturing complexity or lack the necessary performance-to-cost ratio for widespread vehicular deployment. Recent advances in vehicular communication systems have also stimulated the development of alternative antenna technologies to facilitate seamless integration with vehicle structures. For instance, flexible antennas based on advanced substrate technologies offer conformal integration with curved vehicle surfaces while maintaining reliable radiation performance[7,8]. Transparent antennas have also attracted increasing attention due to their capability to be integrated into vehicle windows without affecting visibility, which is particularly beneficial for millimeter-wave vehicular communications[9]. In addition, low-profile and low-windage omnidirectional antenna structures have been investigated to reduce aerodynamic impact and improve system robustness in high-speed vehicular environments[10–12]. These emerging antenna concepts highlight the growing diversity of design approaches aimed at meeting the stringent requirements of next-generation vehicular communication systems.

In response, this work proposes a compact, single-layer FPC antenna that leverages a Sierpinski fractal patch and PRS to achieve enhanced gain and stable circular polarization, while maintaining a planar, low-cost architecture suitable for large-scale automotive integration. The proposed antenna is tailored for V2V and V2I applications within the DSRC band (5.6–6.09 GHz), offering robust circular polarization and high gain to ensure reliable communication in dynamic, multipath-rich environments. Unlike many existing solutions that suffer from complex multilayer designs or limited bandwidth, this work addresses the pressing need for a compact, low-profile, and easily manufacturable antenna. By integrating a Sierpinski fractal array with a dual-layer PRS-based FPC, the design achieves enhanced performance while remaining suitable for seamless integration into modern vehicles.

Recent research has demonstrated significant interest in FPC antennas owing to their high efficiency, substantial gain, and straightforward feeding mechanisms[13]. Consequently, FPC antennas are recognized as a potential remedy for overcoming the challenges associated with V2X services. The antenna structure comprises a feed antenna sandwiched between a PRS and a ground plane. The PRS is placed at a designated height above the ground plane, shaping an air cavity in between. The electromagnetic (EM) waves generated by the radiating antenna undergo multiple reflections within this cavity. When the resonant conditions are met, these waves combine in phase, resulting in highly directive radiation.

On the other hand, metamaterials are artificially created materials by periodically introducing small "unit cells" into a dielectric, making them quasi-homogeneous. This periodic insertion alters the dielectric's macroscopic properties, changing its behavior concerning incident waves. The homogenization concept applies when the unit cell dimensions are smaller than the excitation wavelength, allowing the metamaterial to be perceived as an effective medium. Consequently, the key properties of the material, namely magnetic permeability (μ) and dielectric permittivity (ε), are established. A metasurface is typically designed by systematically arranging electrically small scatterers made of metamaterials in a two-dimensional configuration. These structures harness the advantageous properties of metamaterials, reducing propagation losses and controlling electromagnetic wave propagation by altering boundary conditions[14–20]. Among them, one type is PRS[15,18,20], commonly used as a superstrate to form Fabry–Perot cavities and enhance antenna radiation characteristics.

FPC antennas are extensively utilized in advanced applications, including long-range wireless communication systems[6,13], highly directional data transfer[19], efficient power transmission, and 5G wireless networks. When a portion of the radiated wave escapes the cavity, it creates an in-phase superposition, significantly enhancing the antenna's directivity in the boresight direction. Fabry–Perot resonators (FPR) have gained considerable attention as high-gain radiators due to their straightforward design and simple feeding mechanism, often employing single-fed excitation[21–27]. In[21], a broadband Fabry–Perot antenna is introduced, incorporating a PRS established using an electromagnetic bandgap (EBG) structure and a reactive impedance surface (RIS)-backed rectangular pitch antenna. This design achieves bandwidths of 21.5% (10.02–12.43 GHz) and 24.8% (9.91–12.71 GHz) with high realized gains of 12.05 dBi and 14.3 dBi for single and dual layers of the EBG superstrate, respectively. In[22], an antenna featuring a metasurface demonstrates a maximum gain and a 30% improvement in bandwidth. The gain enhancement is attributed to the in-phase electric field region on the metasurface top layer. Additionally[23], proposes a microstrip patch antenna with a metamaterial superstrate incorporating S-shaped elements to enhance gain characteristics. The antenna operates within a frequency range of 5.65–5.935 GHz, achieving an impedance bandwidth exceeding 0.92% and a gain improvement to 8 dBi, resulting in a peak gain of 10.7 dBi in the direction of maximum radiation. In[25], an EBG cell-embedded antenna system is designed to suppress surface waves, achieving an increased peak gain of 10.15 dBi.

Conventional FPC antennas face a core limitation because they have a limited 3-dB gain bandwidth that becomes more severe when used in CP configurations due to the restricted AR bandwidth. The main cause of this limitation stems from the monotonic reflection phase response of conventional PRS structures which limits the cavity resonance to a specific narrow frequency band. Recent studies have developed PRSs with positive reflection phase gradients to achieve broadband cavity resonance and extended gain bandwidths[26–30]. In[26], an FPC antenna operates over two wide bands using a partially reflective metasurface with magnetic coupling layers and patches. The results confirm 3 dB gain bandwidths of 20.7% (5.7–6.9 GHz) and 10.1% (11.7–12.95 GHz) with peak gains of 12.07 dBi and 13.1 dBi, respectively. In[27], a FPR antenna is proposed, utilizing an aperture-coupled microstrip feeder and an FSS superstrate with a positive reflection phase gradient. The antenna exhibits an impedance bandwidth of 64.4% (8.68–15.12 GHz) and a 3 dB gain bandwidth of 31.9% (8.61–11.80 GHz), with a peak gain of 14.0 dBi. The Fabry–Perot antenna system in[30] demonstrates a 3 dB gain bandwidth of 32.8% (7.9–11 GHz), with a peak gain of 13.67 dBi. The FPC antenna consists of a hexagonal PRS with a positive phase gradient from 7.9 to 10.9 GHz. In[28], a broadband high-gain Fabry–Perot antenna is implemented using an air-loaded slot-coupled microstrip antenna and a PRS with a positive gradient reflection phase, achieving a maximum gain of 10.35 dBi and 31.5%. Operating bandwidth. The existing literature highlights a tradeoff between performance, design complexity, and compactness. It is challenging to find a single design that offers simplicity, compactness, high gain, wide operating bandwidth, and CP performance. Consequently, available scientific publications demonstrate that CP Fabry–Perot antennas continuously face limitations in gain, bandwidth, polarization purity and structural simplicity and compactness. Designing a single antenna to achieve wide AR bandwidth along with high gain and low-profile integration presents a persistent design challenge. Recent antenna research have combined fractal geometries with multilayer and superstrate-based arrays for bandwidth enhancement and miniaturization, and improved gain and directivity through their work[31–36,38,39]. Antennas used in vehicular and intelligent transportation systems (ITS) need to meet strict specifications regarding polarization stability, compact size and dynamic operating condition robustness[34,37,38,39,40,41]. Multiple reported antenna designs in vehicular applications use metasurfaces, multilayer structures and fractal arrays to produce high gain along with circular polarization, but these designs encounter profile height limitations and fabrication complexity which restrict their practical use.

To surpass these constraints this research introduces a small Fabry–Perot cavity antenna which combines a Sierpinski fractal-based 1×2 radiating array with a dual-layer square-ring PRS that produces a positive reflection phase gradient. The proposed design uses a dual-cavity Fabry–Perot resonance system to improve both gain and improve both gain and 3-dB gain bandwidth performance through a single resonant structure which keeps its small size and manufacturing ease. The fractal radiating array enables multi-resonant excitation, which synergistically interacts with the dual-layer PRS to broaden the operational bandwidth and stabilize circular polarization. The proposed antenna design delivers optimal performance between high gain and wide AR bandwidth and compact size and structural simplicity which makes it ideal for dependable V2V and V2I communication systems.

This innovative Sierpinski array-based FPC antenna design makes several important contributions that we summarize below:

- The systematic design and analysis of a compact wideband circularly polarized feeder antenna yield high gain performance together with broad impedance bandwidth and stable axial-ratio (AR) operation in a smaller physical volume.
- Square-ring PRS unit cells undergo rigorous design work and characterization to achieve optimal reflection phase with electromagnetic characteristics that enable broadband Fabry–Perot cavity resonance.
- The combination of the proposed fractal feeder antenna and partially reflective PRS layer produces the first Fabry–Perot cavity that achieves substantial gain and boresight directivity enhancement through constructive cavity interference.
- The implementation of a second Fabry–Perot cavity occurs through the addition of a PRS layer that features a different unit-cell configuration for enhanced 3-dB gain bandwidth extension.
- The research introduces a novel Sierpinski fractal antenna as a dual-cavity Fabry–Perot feeding element that enables multiple resonance points and expanded gain and circular polarization bandwidth.

The subsequent parts of the article are structured as follows: Section II details the proposed design configuration, Section III highlights the design evolution, Section V discusses the working and design analysis of PRS, Section VI is about the parametric study. Section VII brief the simulated and measured results, Section VIII discusses the link budget analysis, Section IX shows the application of the proposed design, and Section X concludes the proposed work.

Proposed design configuration

The antenna design and optimization were performed using CST Microwave Studio (MWS), a full-wave electromagnetic simulation tool known for its accuracy in modeling complex antenna structures. The methodology involved iterative design of the Sierpinski fractal patch integrated with a PRS-based FPC to achieve the desired high gain and stable circular polarization within the DSRC band. Simulations included detailed analysis of gain, AR, bandwidth, and radiation patterns under realistic boundary conditions. The design was subsequently fabricated and experimentally validated, confirming the simulation results and demonstrating practical applicability for vehicular communication systems. This structured approach ensures that each stage from design through validation directly addresses the performance challenges and integration requirements of V2V and V2I antennas. The antenna structure and dimensions are exposed in Fig. 1(a-c) and Table 1, respectively. The proposed design comprises a two-element array of a Sierpinski carpet antenna array with truncated diagonal corners for achieving circular polarization features as given in Fig. 1(a).

The design has a feeding network of a three-section quarter-wave transformer combined with a T-junction power splitter as displayed in Fig. 1(a). Given in Fig. 1(b), the PRS contains a 9×7 periodic unit cell array with a periodicity of P = 22 mm. The PRS overall substrate (made of Rogers 5880, $\varepsilon_r = 2.2$, $\tan\delta = 0.0009$) has a width and length of $Lsub = 198$ mm and $Wsub = 154$ mm, respectively. The antenna substrate and ground plane have the same dimensions as those of the PRS. While each Sierpinski carpet has a width and length of $Wp = 24$ mm and $Lp = 24$ mm, respectively. The corners of the patch are cut by $W_{SQ} = 4$ mm to achieve circular polarization performance and improve the impedance matching and AR bandwidth. Fig 1c shows the 3D exploded view of the proposed design. The PRS surface is positioned on the radiating patch at a distance *d*, which is also the air gap between the radiating element and PRS Table 1.

Design equations

Radiating antenna design equations

The proposed antenna design incorporates two primary elements: a Sierpinski fractal structure and a PRS. These elements are derived from specific mathematical formulations. The radiating element is constructed using the Sierpinski carpet fractal principle, which begins with a square shape referred to as the initiator (iteration 0). The

Dimensions	Values	Dimensions	Values
W_p	24	*L1*	32.3
L_p	24	*W1*	1.9
WSQ	5	*L2*	5.7
L0	3.8	*W2*	2.85
W0	11.4	*L3*	4.28
L01	7.6	*W3*	1.52
W01	9.3	*L4*	7.6
L02	7.6	*W4*	3.65
W02	8.8	*L5*	6.37
Lsub	198	*Wsub*	154

Table 1. Optimized dimensions of the antenna design (mm).

dimensions of the individual element are calculated using foundational equations commonly employed in the design of rectangular patch antennas. The design of the target antenna starts with a rectangular patch, which operates at a 5.8 GHz resonant frequency. By using the following equations for the values of relative permittivity (ε_r) = 2.2, resonance frequency (f_r) = 5.9 GHz, height of the substrate (h) = 1.6 mm and speed of light (c) = 3×10^8 m/s, the rectangular patch dimensions are calculated as following (1)[53,54]:

$$W = \frac{c}{2fr\sqrt{\frac{\varepsilon_r}{2}}} \tag{1}$$

where '*W*' is the width of the patch. The effective dielectric constant is computed using (2):

$$\varepsilon_{\mathrm{reff}} = \frac{\varepsilon_r + 1}{2} + \frac{\varepsilon_r - 1}{2}\left(1 + \frac{h}{W}\right)^{1/2} \tag{2}$$

The patch effective length is derived as (3)

$$L_{eff} = \frac{c}{2fr\sqrt{\varepsilon_{reff}}} \tag{3}$$

The fringing effect is estimated using (4) :

$$\Delta L = 0.412h\frac{\left(\frac{W}{h} + 0.264\right)(\varepsilon_{\mathrm{reff}} + 0.3)}{\left(\frac{W}{h} + 0.8\right)(\varepsilon_{\mathrm{reff}} - 0.258)} \tag{4}$$

Thus, the resultant total patch length of the design is given as (5):

$$L = L_{eff} + 2\Delta L \tag{5}$$

The iteration process divides the square into nine equal squares with a three-by-three grid, which is followed by adding a square slot in the center of the radiating element. To perform this iteration process, an iterative function system (IFS) is used to describe the Sierpinski fractal structure. It creates a series of self-affine based on the transformation *w*, which is defined as (6)[42,43]:

$$w_i\begin{bmatrix} x \\ y \end{bmatrix} = \begin{bmatrix} a & b \\ c & d \end{bmatrix}\begin{bmatrix} x \\ y \end{bmatrix} + \begin{bmatrix} e \\ f \end{bmatrix} \tag{6}$$

Here, the matrix $\begin{bmatrix} a & b \\ c & d \end{bmatrix}$ represents the rotation coefficient, while the vector $\begin{bmatrix} e \\ f \end{bmatrix}$ represents a translation coefficient of the coordinates (x,y). Each transformation w_i is applied to the initial geometry A (the initiator, which is the original square in this case). Note that the *w(A)* represents a system of linear affine transformations. The new geometry is generated by applying each transformation w_i to the initial geometry A and then combining the results. This can be expressed by the Hutchinson operator (7):

$$w(A) = \bigcup_{i=1}^{N} w_i(A) \tag{7}$$

In the context of the Sierpinski fractal, the transformation w_i corresponds to the mappings that scale and translate the initial square into the eight smaller squares. By iteratively applying these transformations to the resulting geometries, the fractal structure emerges, exhibiting its characteristic self-similarity at every scale.

Design equations for partially reflective surface (PRS)

The geometry and dimensions of the PRS unit cell are illustrated in Fig 5a. It consists of two square patches with a gap *w* between them. Here, *Le* and *Li* represent the widths of the outer and inner square patches, respectively. *P* denotes the length of the substrate (Periodicity). Current flow originates from the ring's ability to conduct when a magnetic field is applied perpendicular to the square patch. Mutual capacitances result from the dielectric gaps between the square patches, and the current passing through them allows the patches to function as an inductor. As a result, a parallel LC tank circuit will be an equivalent representation of the PRS unit cell[45]. The resonant frequency can be calculated as (8):

$$f_o = \frac{1}{2\pi\sqrt{LC}} \tag{8}$$

where *C* represents the equivalent capacitance, while *L* is the effective inductance due to both square patches (9).

$$L = \frac{4.86\mu_0}{2}\left(p - W1 - g\right)\left[ln\left(\frac{0.98}{\rho}\right) + 1.84\rho\right] \tag{9}$$

where,

ρ is the filling factor, it's given by (10):

$$\rho = \frac{W1 + g}{p - W1 - g} \tag{10}$$

The effective capacitance is given by (11):

$$C = \left(p - \frac{3}{2}\left(W1 + g\right)C_{pul}\right) \tag{11}$$

where C_{pul} is the per unit length capacitance between the patches, which is computed using (12):

$$C_{pul} = \varepsilon_0\varepsilon_{eff}\frac{K\left(\sqrt{1-k^2}\right)}{K(k)} \tag{12}$$

where ε_{eff} is the effective dielectric constant expressed as (13):

$$\varepsilon_{eff} = \frac{\varepsilon_r + 1}{2} \tag{13}$$

K(k) stands for the complete elliptic integral of the first kind, with k defined as (14):

$$k = \frac{g}{g + 2W1} \tag{14}$$

These equations are instrumental in determining the lumped equivalent model of the PRS unit cell.

Design evolution

The thorough design methodology of the suggested antenna is depicted in Fig. 2 (Ant 1-Ant 7). The antenna design is developed through a systematic seven-step process, beginning with the simulation of a simple rectangular patch. The first step (Ant 1) involves a basic rectangular patch. In the second step (Ant 2), the first iteration of the Sierpinski carpet is applied to the patch. In the third step (Ant 3), the Sierpinski carpet structure is extended to the remaining area, resulting in the second iteration. Additionally, along the x-axis, the proposed Sierpinski-based antennas are arranged to create a two-element linear array, as shown in step four (Ant 4), to enhance the antenna's gain. In the fifth step (Ant 5), CP is achieved by truncating the patch corners. Subsequently, in step six, the optimized design of Ant 5 is combined with an FSS having only a top layer to form an FPC. The cavity is constructed using a 9 × 7 unit cell array on the superstrate. Finally, in step seven (Ant 7), the FPC antenna is further enhanced by adding a bottom PRS layer on the substrate. The impedance matching, represented by reflection loss S_{11}, circular polarization in terms of AR, and broadside gain for various antenna configurations (Ant1–Ant7) are presented in Fig. 3 (a-b).

The simulated reflection coefficients (S_{11}) for each step are shown in Fig. 3(a). The initial rectangular patch antenna resonates at 5.67 GHz. Incorporating the first iteration of the Sierpinski carpet slot improves both impedance and AR bandwidth, resulting in two resonant bands at 5.17GHz and 5.6 GHz. The second iteration of the Sierpinski carpet slot maintains resonance within similar frequency bands as the first iteration (Ant 2). The two-element array configuration (Ant 4) demonstrates resonance around 5.5 GHz and 5.93 GHz with a broader bandwidth. This slight shift in the operating band toward higher frequencies is due to the fractal geometry, which provides a longer effective path for current flow, thereby reducing the resonant frequency. The patch corners are then truncated to improve circular polarization. The design in Ant 5 combines both the truncated corner patch and the Sierpinski fractal geometry to enhance AR and impedance matching by overlapping the individual resonances of the patch. Meanwhile, Ant 6 and Ant 7 exhibit similar reflection coefficient responses. Fig 3(b) shows the simulated gain of the design. The basic patch antenna (Ant 1) has a narrow impedance bandwidth

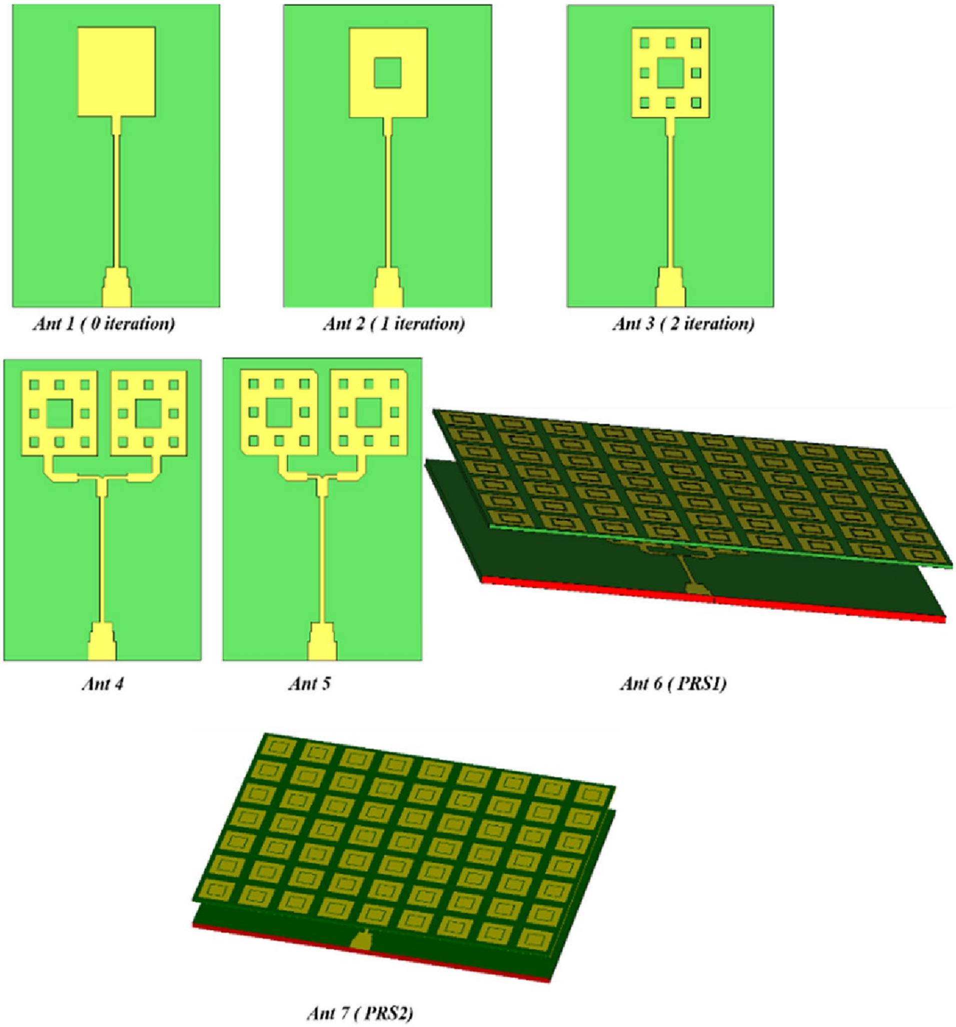

Fig. 2. Evolution steps of the proposed FPC antennas.

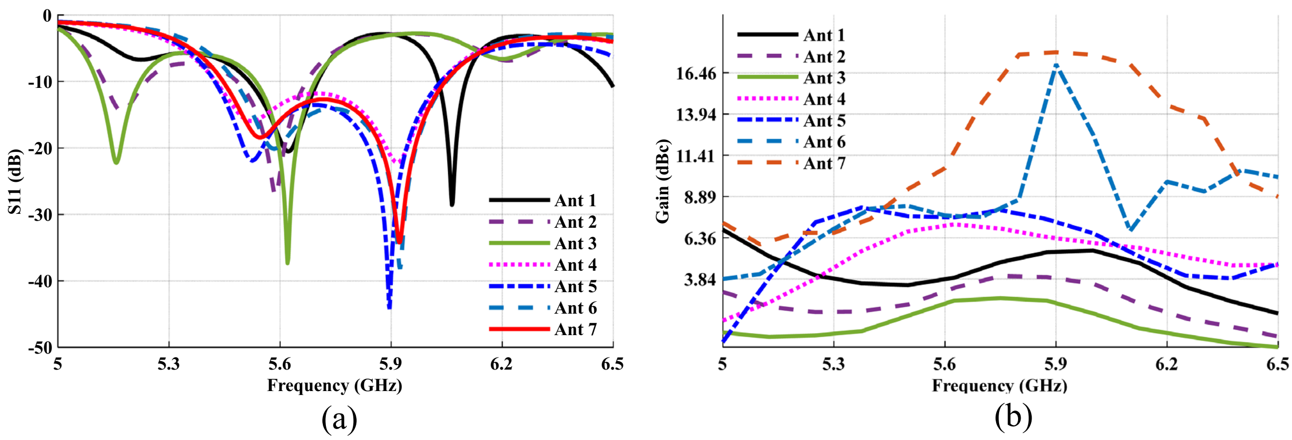

Fig. 3. Proposed antenna results in each successive step for (**a**) reflection coefficient, and (**b**) gain.

around 5.67 GHz, linear polarization, and a gain of 5.6 dBi. In contrast, the patch antenna with the first and second iterations of the Sierpinski carpet fractal geometry (Ant 2 and Ant 3) shows a reduced gain of less than 2.8 dBi. The two-element array (Ant 4), excited through an optimized feeding network, demonstrates a significant gain enhancement by effectively combining the individual resonances of the array elements. While

Ant 5 has no noticeable impact on the gain, the introduction of a single upper PRS layer in Ant 6 significantly increases the gain to 16.48 dBi, with a relatively narrower bandwidth response. Ant 7 adds a second layer, underside of the PRS substrate, further increasing the gain up to 17.72 dBi while maintaining a wideband response.

Working and design analysis of PRS

When a PRS is positioned above the radiating element, the PRS and the ground plane, which are separated by a specific distance (Fig. 4), create an FP cavity.

The small antenna's emitted radiation undergoes several reflections between the PRS and the ground plane, with each reflection diminishing in amplitude. This series of reflections culminates in constructive interference, substantially enhancing the antenna's directivity in the boresight direction. Consequently, the resonant condition within the FP cavity, defined by a height *d* (the separation of the ground plane from the PRS), can be expressed as (17)[46,47]:

$$\varphi_r = \frac{4\pi d}{c} f_r - 2N\pi - \varphi_{GND}, \mathrm{N} = 0,1,\ldots \tag{15}$$

In (17), N is an integer that characterizes the order of resonance and is taken to be zero, f_r is the operating frequency, φ_{GND} is the phase introduced by the ground plane, and *c* is the velocity of light in space. This equation indicates that the effectiveness of the cavity is considerably altered by the height *d* of the cavity and the reflection properties of the PRS top interface. Maximum gain and directivity are achievable in the propagation direction when the resonance condition of the cavity is met. This condition is described in (18)[46,47]:

$$d = \frac{c}{4\pi f_r} \left(\varphi_r + \varphi_{GND} + 2N\pi\right) \tag{16}$$

The distance *d* leads to constructive interference, and the waves emanating from the PRS are in phase. A high reflectivity of the PRS top surface with a linear increase in its phase response implies a maximum gain in certain frequency bands. The expression for the gain in the direction of radiation (for $\varphi = 0°$), as a function of the reflection coefficient magnitude, is given by (19)[46,47].

$$G = \frac{1+R}{1-R} \tag{17}$$

When the reflection coefficient of the PRS approaches unity, the gain of the antenna becomes significantly higher due to the high reflectivity. However, as the reflection coefficient increases, the radiation bandwidth narrows, resulting in a trade-off between gain and bandwidth. This relationship is expressed mathematically in Eq. (18) below:

$$BW = \frac{\lambda_0}{2\pi d} \frac{1-R}{\sqrt{R}} \tag{18}$$

Optimizing the reflection characteristics of the PRS, including both phase and amplitude, is crucial to gain a balance between high gain and wide radiation bandwidth. It is widely recognized that higher reflection amplitudes of the PRS lead to increased directivity, but this improvement typically results in a reduction of the bandwidth[52]. Consequently, designing FP cavity antennas that simultaneously achieve both wideband operation

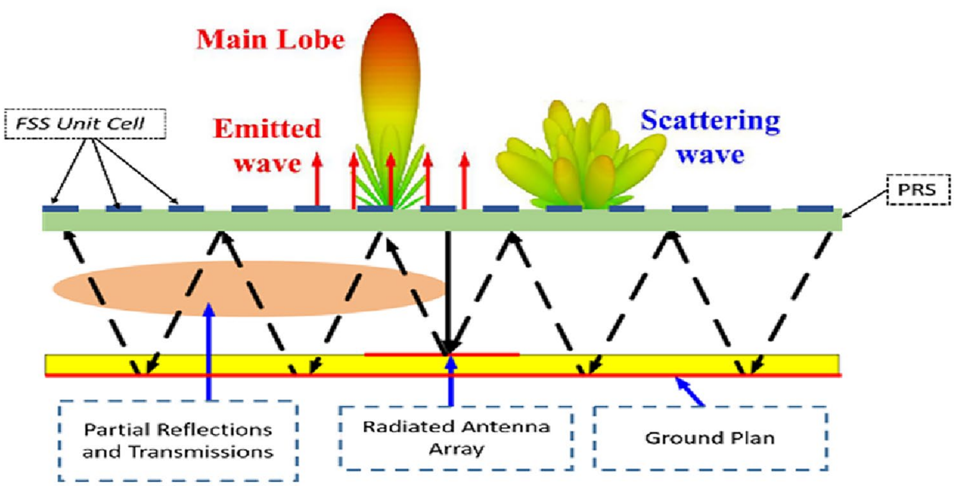

Fig. 4. Fabry–Perot Cavity working Principle.

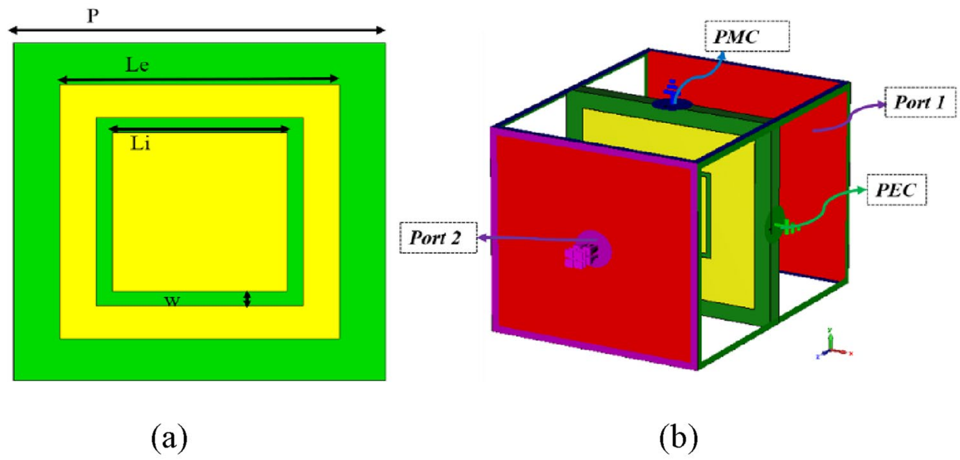

Fig. 5. Geometry of the unit cell PRS1.

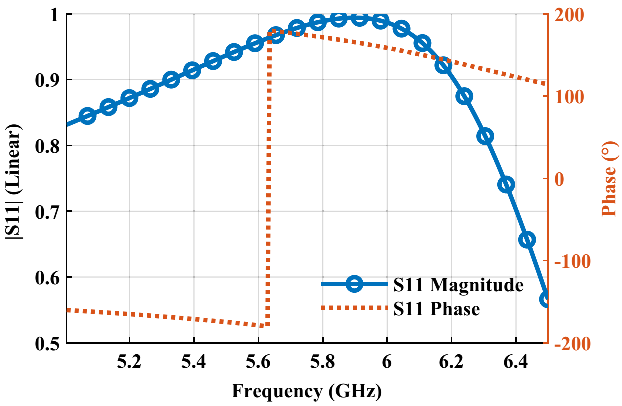

Fig. 6. Reflection coefficients magnitude and reflection phase in degrees for the optimized unit cell.

and high gain characteristics presents a significant design challenge. A variety of PRS unit cell configurations exists, with common examples including square patches and square apertures. In this design, a dedicated unit cell is proposed to create a PRS functioning at approximately 5.9 GHz. The unit cell employs a square slot-loaded patch (SSLP) configuration, where a square slot of width *Li* is integrated into a conventional square patch (CSP) of width *Le*. This modification enhances and regulates the bandwidth of the positive reflection phase gradient. Furthermore, the square slot provides an additional parameter for tuning both the phase and magnitude of the PRS reflection coefficient. By combining these two distinct PRS configurations, an artificial reflection phase can be achieved, closely approximating the ideal phase response.

Unit cell of single top surface PRS

The structure of the proposed unit cell of single surface PRS is depicted in Fig. 5(a-b). The proposed unit cell (PRS1) is printed on the top side of a Rogers5880 substrate (ε_r= 2.2, $\tan\delta = 0.0009$) with a thickness of 1.575 mm. Fig 5(a) presents the top view of the unit cell. Fig 5(b) illustrates the unit cell simulation setup in CST MWS, with port 1 and port 2 aligned along the z-axis and placed at a specified distance from the unit cell. Electric and magnetic wall boundaries are applied along the x-axis and y-axis, respectively.

The reflection magnitude and reflection phase of the optimized unit cell are illustrated in Fig. 6. A reflectivity approaching 1 is achieved, accompanied by a reflection phase of 168°. Once optimized, the final sizes of the two concentric metallic squares are found to be Le = 18.6 mm, Li = 8.2 mm, and w = 1 mm. The period of the cell is fixed at P = 22mm. From the phase value of the reflection coefficient, the height of the Fabry–Perot cavity can be calculated for the operational frequency of around 5.9 GHz. Using φ_r = 168.78° in the reflection coefficient phase equation for the PRS superstrate and φ_{GND} = 180° (the phase of the ground plane, a perfect electric conductor), the height *d* is calculated to be 24.65 mm. These dimensions are sufficient when using PRS1 alone. However, to further improve gain, bandwidth, and beam width, PRS2 is introduced. In PRS2, the dimensions of PRS1 are slightly optimized, enabling the achievement of maximum gain, bandwidth, and beam width.

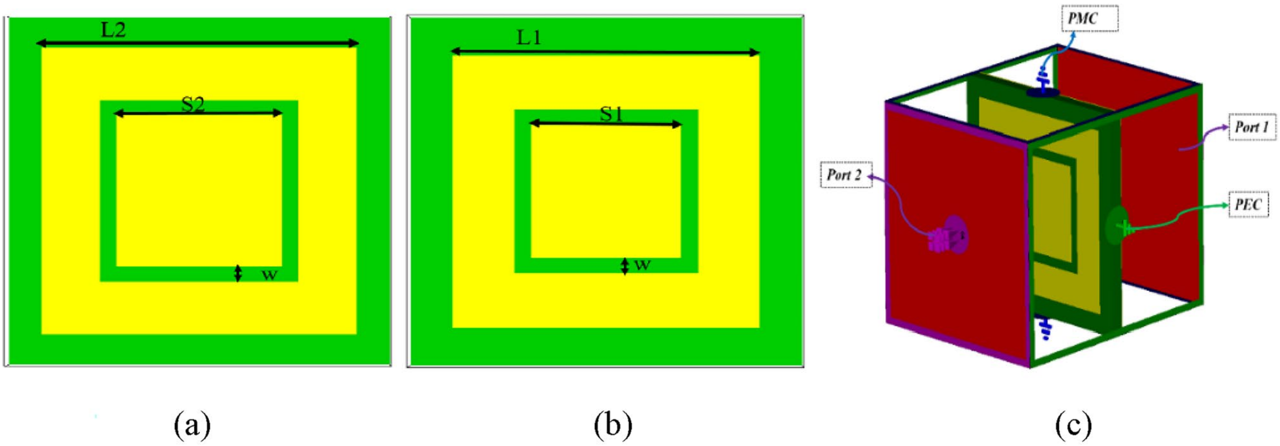

Fig. 7. Geometry of the unit cell PRS2: (**a**) Top surface, (**b**) Bottom surface and (**c**) Step view.

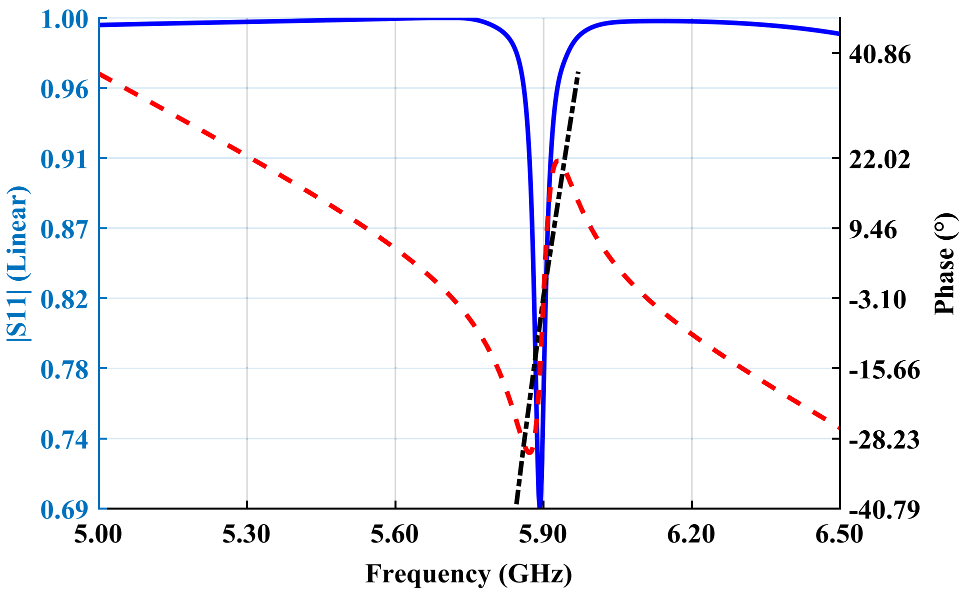

Fig. 8. Reflection coefficients magnitude and reflection phase in degrees for the optimized unit cell.

Unit cell of positive phase gradient, double surface PRS (PRS2)

The principle used to design the two surfaces PRS elementary pattern is similar to the literature demonstrated in[30]. The study has shown that one or more resonance points with a growing reflection phase can be created between two PRS cells of similar shapes but different dimensions. Our goal is to form a cavity between two PRS layers using the same PRS cell previously employed to construct the single layered PRS, but with different dimensions. Fig 7 illustrates the configuration of the dual-layer cell under consideration. Observing Fig. 8, we can see that the variation in the reflection phase of the proposed unit cell has positive slope within the band of 5.87 GHz to 5.93 GHz. The magnitude of the reflection coefficient exceeds 0.69, while the phase varies from −28° to 22° across the entire band. Notably, at 5.9 GHz, the phase is equal to −3.1°. Thus with the mentioned dimensions, the PRS has demonstrated the required performance.

Parametric analysis

Here, a thorough parametric analysis is presented to assess the influence of key parameters on the FP antenna's overall performance. These parameters include the impact of changing dimensions of the upper and lower PRS unit cells, the impact of changing the corner truncation on the reflection coefficient and axial ratio of the radiating element, and the influence of varying the separation distance between the PRS layers and the radiating array.

Impact of varying first PRS unit cell (PRS1) dimensions on S_{11} and phase

As shown in Fig. 9, a parametric study is conducted to analyze the impact of each unit cell dimension on the reflection magnitude and phase. From Fig. 9 (a-b), it is observed that varying *Le* and *Li* (the widths of the outer and inner square patches, respectively) influence the reflection phase, but no significant effect is observed for the reflection magnitude. Conversely, adjusting the gap *w* between the patches affects both the S_{11} magnitude and phase within the operating frequency band (Fig. 9(c)).

Impact of varying second PRS unit cell (PRS2)dimensions on S_{11} and phase

It is important to emphasize that optimizing the reflection characteristics of the design is crucial for achieving a wider bandwidth and higher gain along the operating band. Here *L1* and *S1* represent the widths of the outer and inner square patches of the top surface respectively and *L2* and *S2* represent the widths of the outer and inner square patches of the bottom surface respectively.

As shown in Fig. 10, the effects of the unit cell dimensions on the reflection magnitude and phase are highlighted. From Fig. 10 (a), it is observed that varying *L1* and *L2* have no significant effect on the phase and magnitude of the reflection coefficient. Given in Fig. 10 (b), varying *S1* and *S2* highly affect the reflection magnitude as well as the position and the frequency band of the positive phase gradient at 5.9 GHz. Fig 10(c)

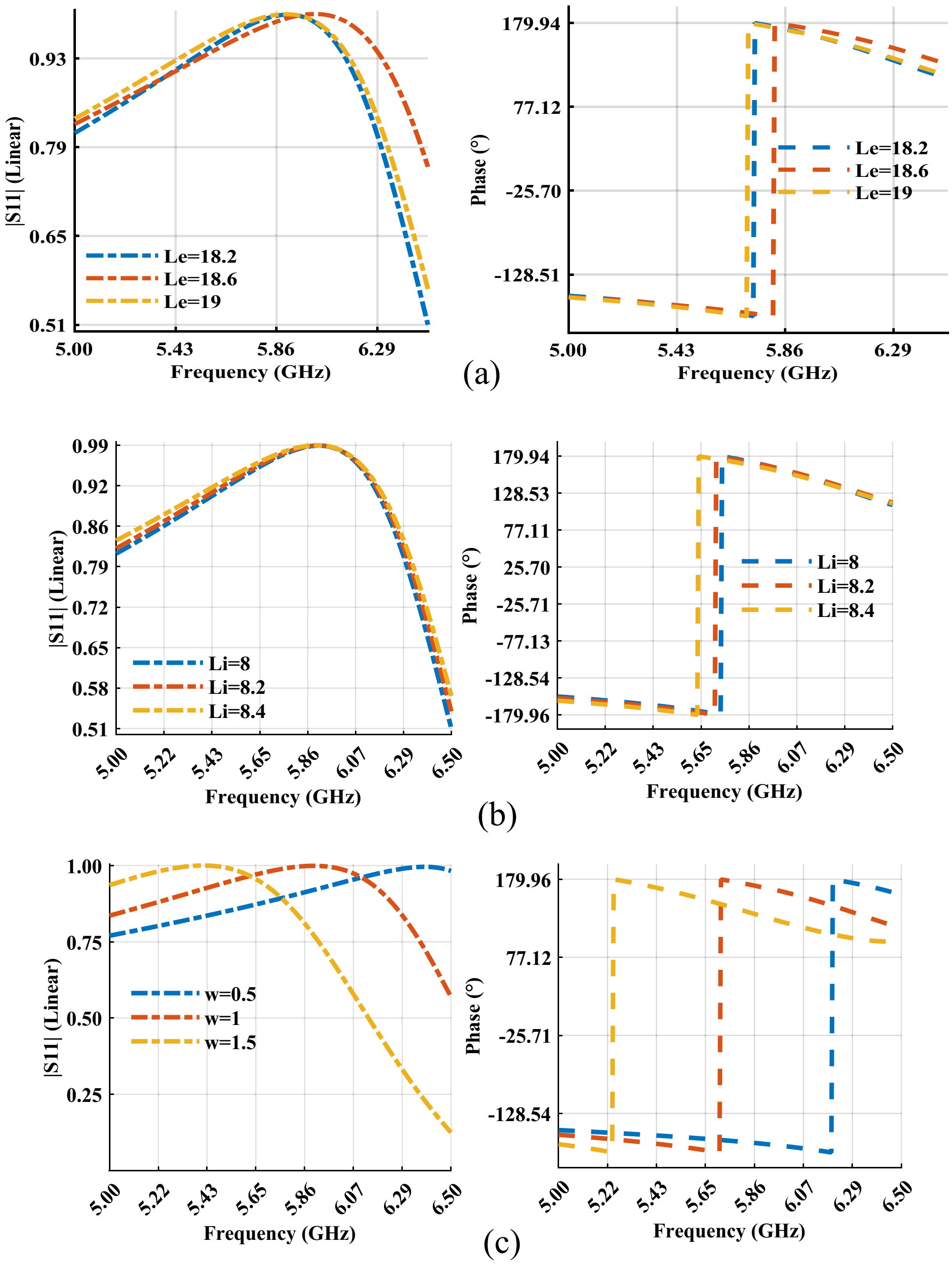

Fig. 9. Reflection coefficients magnitude and reflection phase in degrees for different parameters of Unit cell 1.

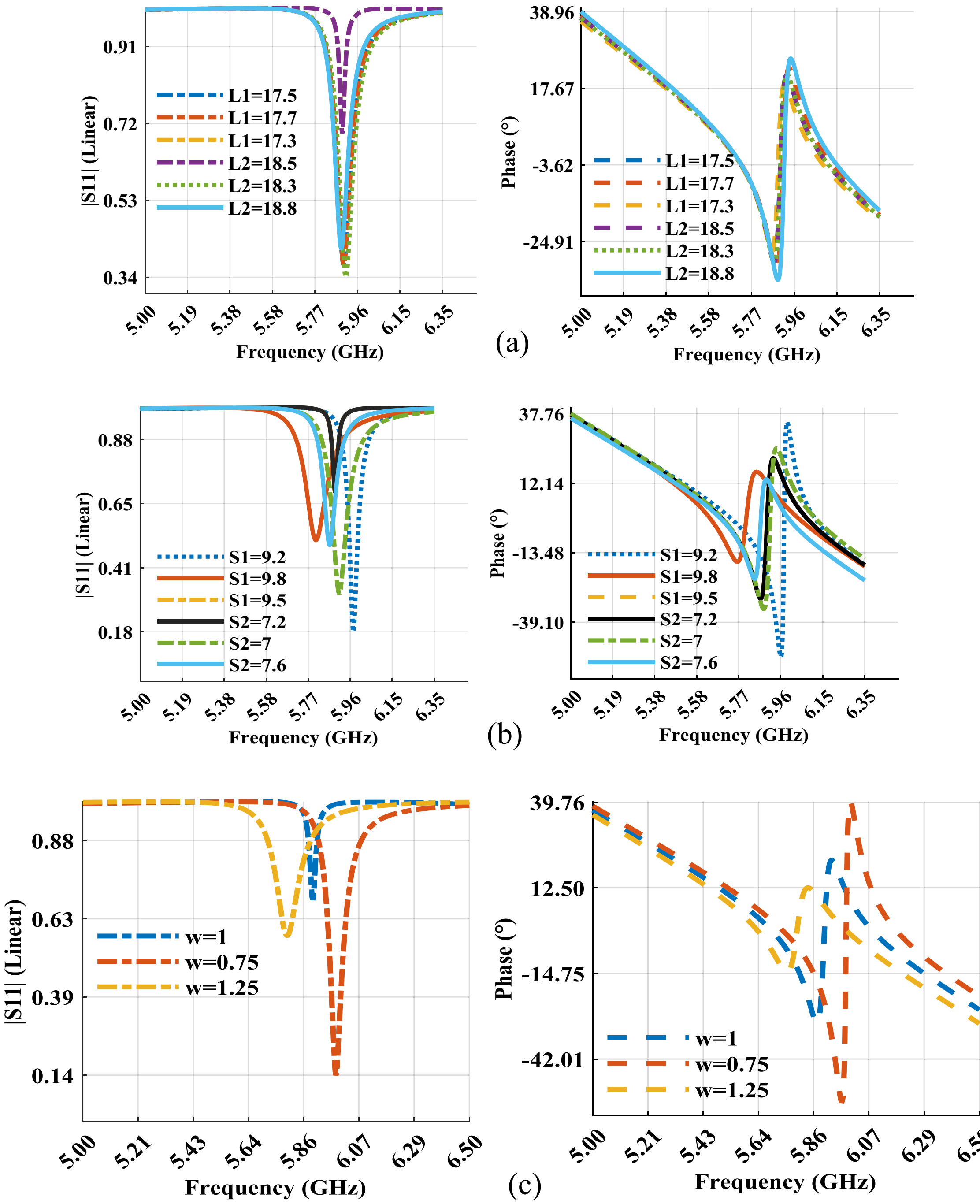

Fig. 10. Reflection coefficients magnitude and reflection phase in degrees for different parameters of the unit cell 2.

shows that changing the gap between the patches also affects the reflection magnitude and the phase gradient of the proposed design. The best response is achieved at $w = 1$mm. The optimal distance between the two layers is set to $d = 25$ mm, and the optimized dimensions (mm) are $L1 = 17.3$ mm, $L2 = 18.3$ mm, $S1 = 9.5$ mm, $S2 = 7.2$ mm, and $w = 1$mm.

Impact of corner truncations of the radiating antenna on impedance matching and axial ratio

To improve the AR bandwidth the corners of the patches are truncated. This configuration exhibits a significant impact on results in terms of impedance matching and enhancing 3 dB AR in the desired frequency band. Figs12(a) and (b) show that gradually increasing the truncation of radiating elements corner improve the upper band matching and AR band width. The maximum improvement is achieved at the *WSQ* of 5 mm. Beyond this value, a degradation is noticed in the AR performance, thus a $WSQ = 5$ mm is the final selected value for the corner truncation of the radiating elementsFig. 11.

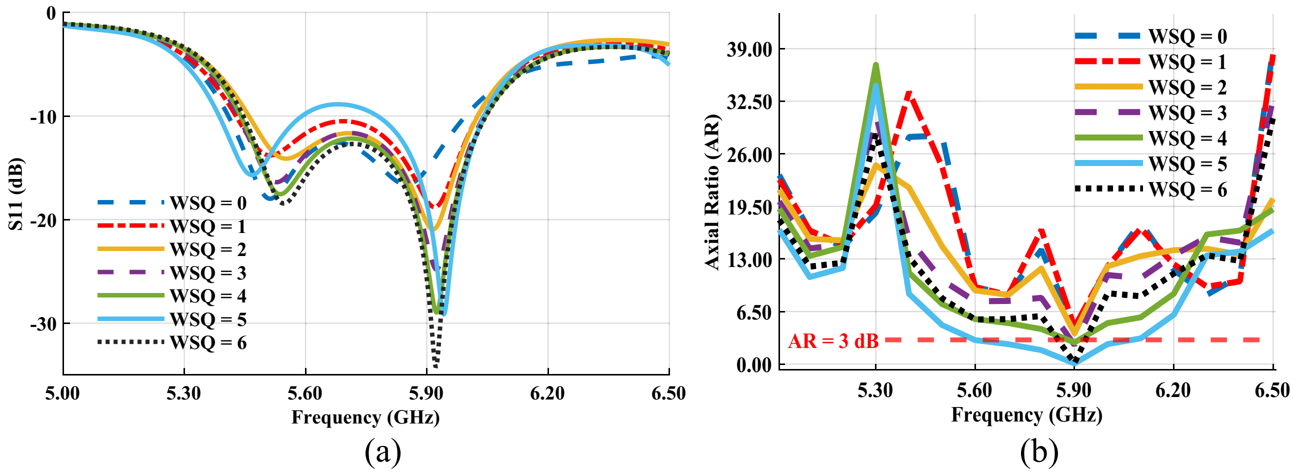

Fig. 11. Impact of changing the values of truncated edges on the axial ratio.

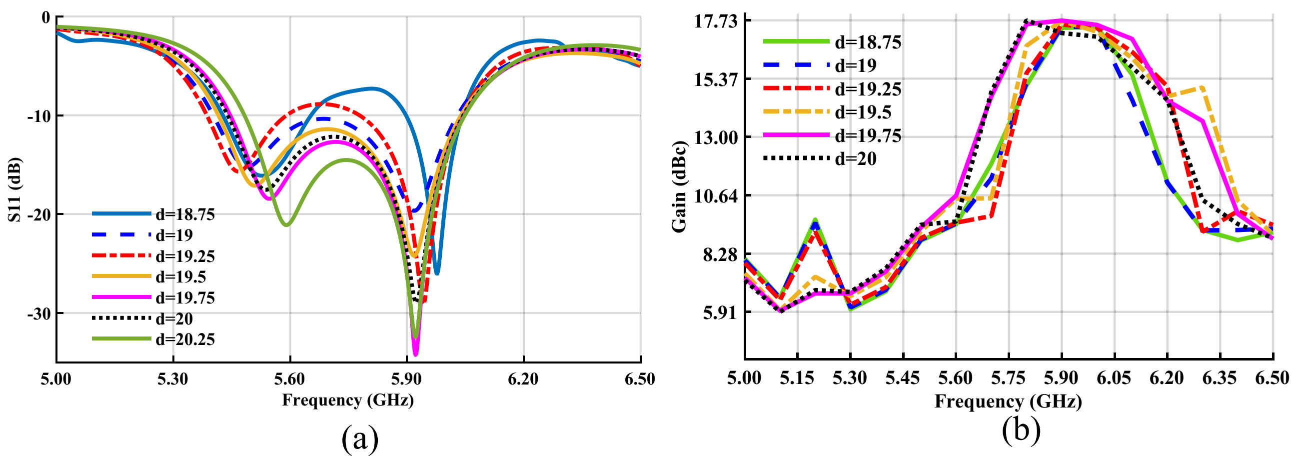

Fig. 12. Effect of d1 variation on (**a**) S11 and (**b**) gain of FP antenna.

A parametric analysis is also conducted on the reflection coefficient and gain of the design, investigating the effect of the separation distance (*d*) between the PRS layers and the antenna element. Significant enhancements in gain and directivity are observed when the PRS superstrate is positioned at an optimal distance above the ground plane of the radiating antenna. Figs 12(a) and (b) illustrate the impact of *d* on the S_{11} and gain of the FP antenna with a single PRS layer. The results in Fig 12 demonstrate that modifying the height (*d*) significantly affects both the values of maximum gain and impedance matching. At $d = 19.75$ mm, a maximum matching and high gain is attained.

Simulated and measured results
S-parameters and gain
The proposed antenna's performance is characterized by analyzing its reflection coefficient (S_{11}), AR, broadside gain, current distribution on the radiating element and PRS, and radiation patterns. These simulated results are subsequently validated through experimental measurements. For the final prototype fabrication, the air gap between the radiator and the PRS is precisely controlled using polyurethane foam with the specified thickness. To minimize insertion losses, the inner portion of the foam is carefully removed. An SMA (Sub Miniature version A) connector is utilized to feed the antenna. Fig 13(a) and (b) presents photographs of the fabricated prototype without PRS and with PRS respectively. Fig 14(c) shows the far-field measurements in the anechoic chamber. Fig 13(d) shows the measured reflection coefficient through Vector Network Analyser (VNA), while Fig. 13(e) shows the complete measurement setup for far-field measurement.

Fig 14(a) illustrates the S_{11} simulated and measured results of the antenna, revealing a broadband performance for a referenced −10 dB impedance bandwidth spanning from 5.47 to 6.1 GHz. The minor discrepancy between the simulated and measured results is likely attributed to cable losses and manufacturing tolerances. The wideband response is achieved through the combined effects of the fractal geometry, truncated patch resonances, and the effective integration of the optimized PRS unit cells. Fig 14(b) displays the simulated and measured broadside

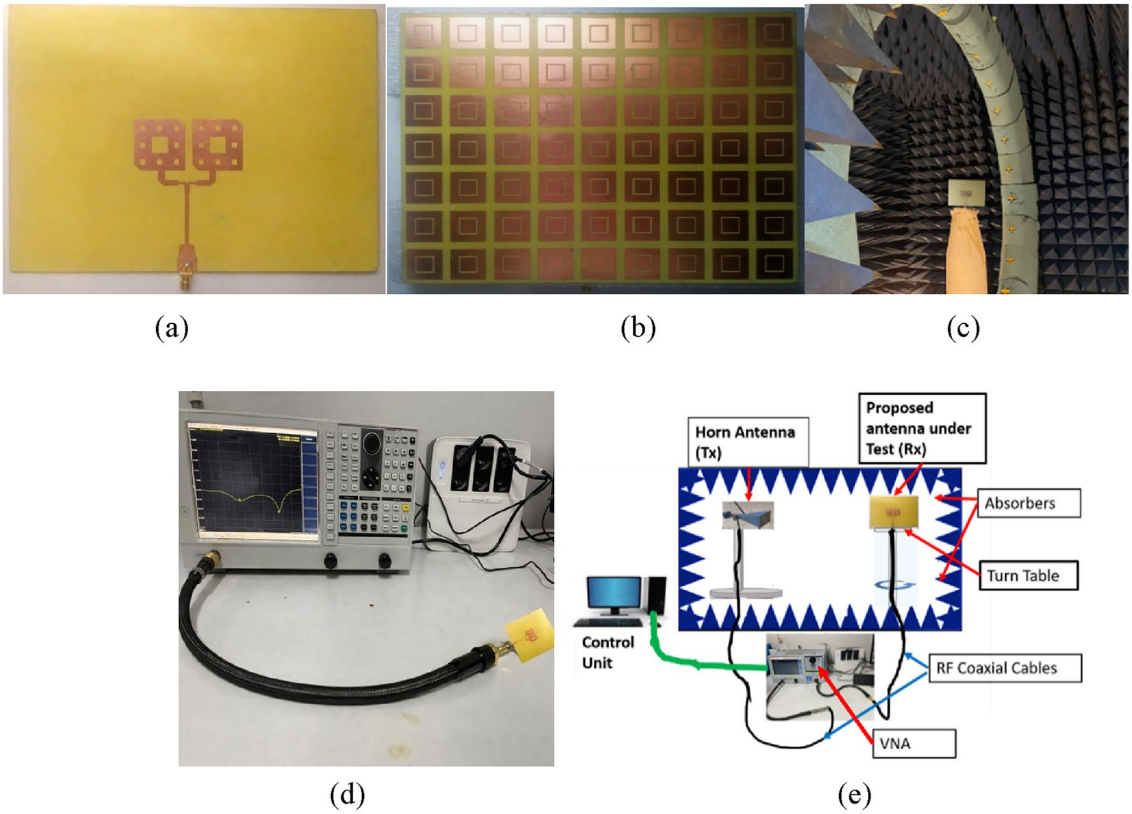

Fig. 13. Fabricated prototype of the proposed Antenna: (**a**) Feeder antenna array, (**b**) PRS Layer, (**c**) Antenna mounted in the anechoic chamber, (**d**) Antenna connected to VNA, and (**e**) Far-field measurement Setup.

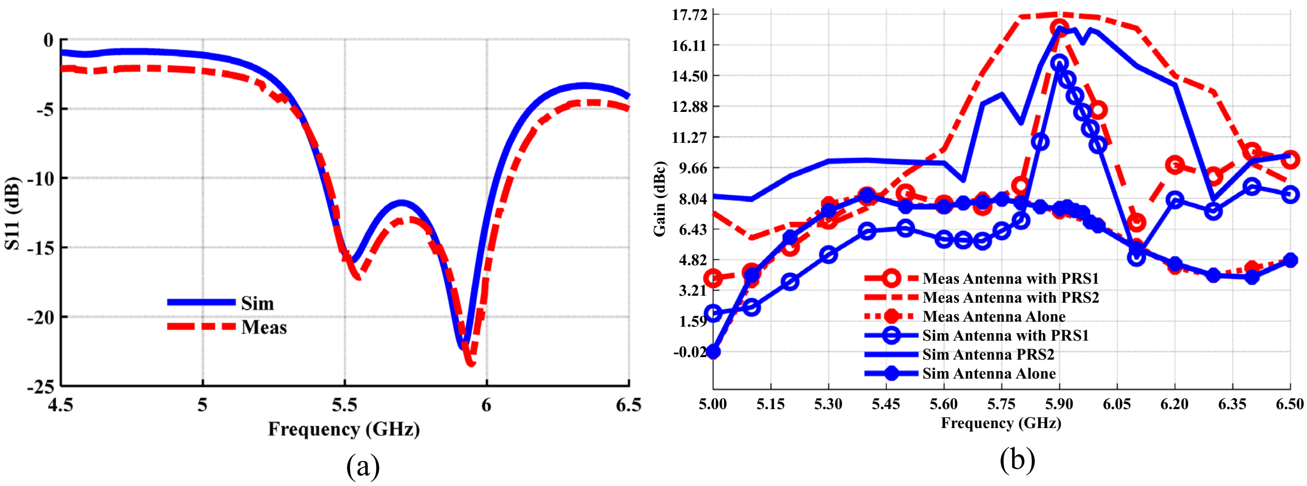

Fig. 14. Measured and simulated values of the design (**a**) reflection coefficient and (**b**) gain of the design.

gain for the various configurations of the proposed design, including the single-element antenna, the FP antenna with a single PRS, and the FP antenna with a double PRS. As evident from the figure, the antenna without the PRS achieves a modest gain of 7 dBc. In contrast, the antenna with a single PRS exhibits significantly higher gains, with simulated and measured values of 15.3 dBc and 16.6 dBc, respectively. The addition of a second PRS further enhances the gain, yielding simulated and measured values of 17 dBc and 17.72 dBc, respectively, at 5.9 GHz. The experimental outcomes are in close alignment with the simulations, with slight deviations that are likely caused by substrate losses and power dissipation in the foam layer used to maintain the cavity thickness.

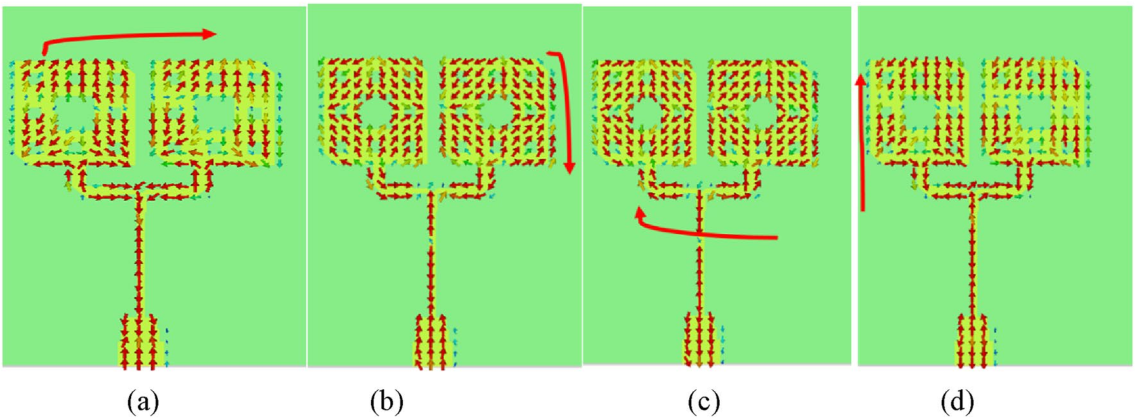

Fig. 15. The current distribution of the proposed feeder antenna at 5.9 GHz : (**a**) 0°, 90°, 180°, and 270° phases respectively.

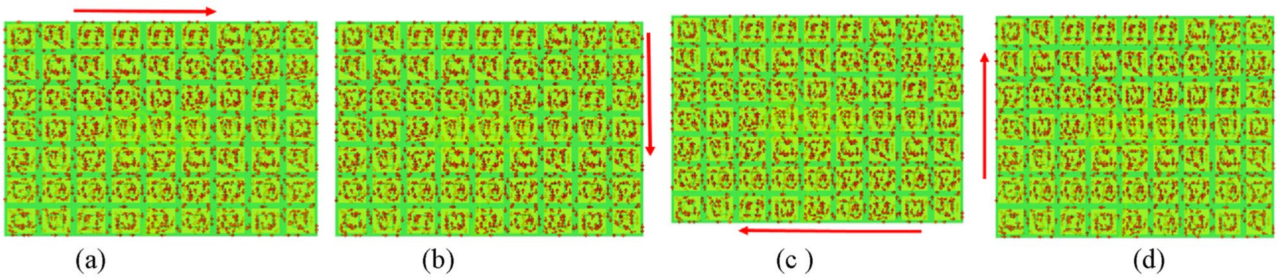

Fig. 16. The current distribution of the proposed Fabry Perot antenna at 5.9 GHz : (**a**) 0°, 90°, 180°, and 270° phases, respectively.

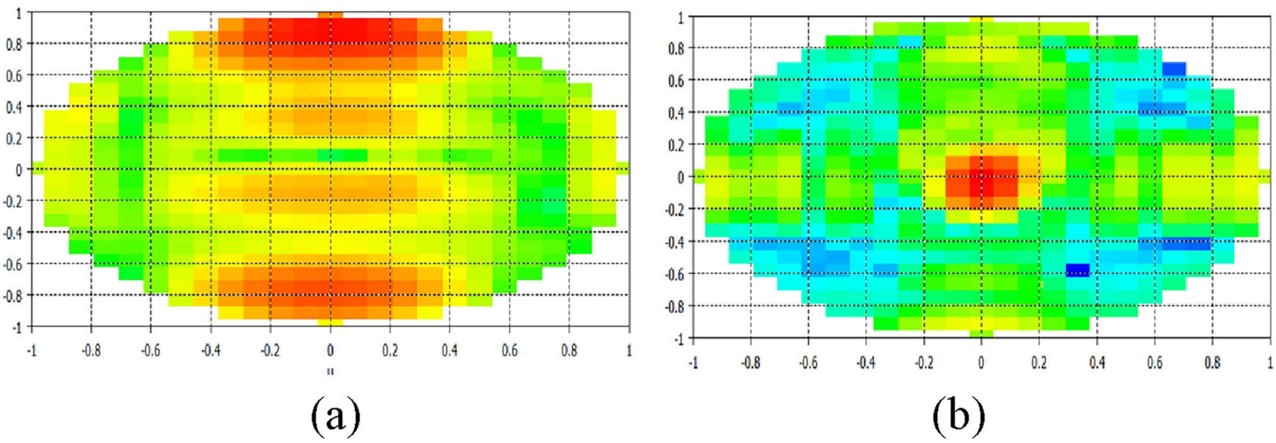

Fig. 17. The electric field distributions at 5.9 GHz of the antenna (a) without and (**b**) with the PRS layers.

Current distribution of the proposed design

This section details the current distribution of the radiating elements (antenna array) and PRS. The current distribution mechanism is highly helpful in explaining the AR performance of the proposed design. The current distribution on the designed antenna at 0°, 90°, 180°, and 270° is given in Figs. 15(a-d) respectively. The clockwise rotation of the radiated field confirms that the antenna exhibits left-hand circular polarization (LHCP). Figs 16(a-d) show that adding PRS layers does not alter the CP performance of the design, and the same impact is visible from the current distribution on the PRS as well. To analyze the gain performance due to the PRS, the current distribution is computed at 5.9 GHz, as given in Fig. 17. The PRS functioned as a lens, concentrating the antenna's electric field in the broadside direction, which led to a significant improvement in the antenna gain. Figs 17 (a) and (b) show the 2D current distribution of the design at 5.9 GHz. It is seen that adding the PRS highly increases the directivity of the design.

Radiation pattern

The far-field patterns of the fabricated prototypes of the proposed feeder antenna array and FPC antenna are simulated and measured at 5.9 GHz for Phi = 0˚ and Phi = 90˚. Figs 18 (a-f) illustrates the radiation patterns in the E-plane and H-plane, obtained through simulation and measurement, alongside the 3D radiation pattern at 5.9 GHz. A strong agreement between the simulated and measured results is observed. The radiation pattern of the feeder antenna without the PRS layer (shown in Figs. 18(a-b)) exhibits omnidirectional behavior, making it

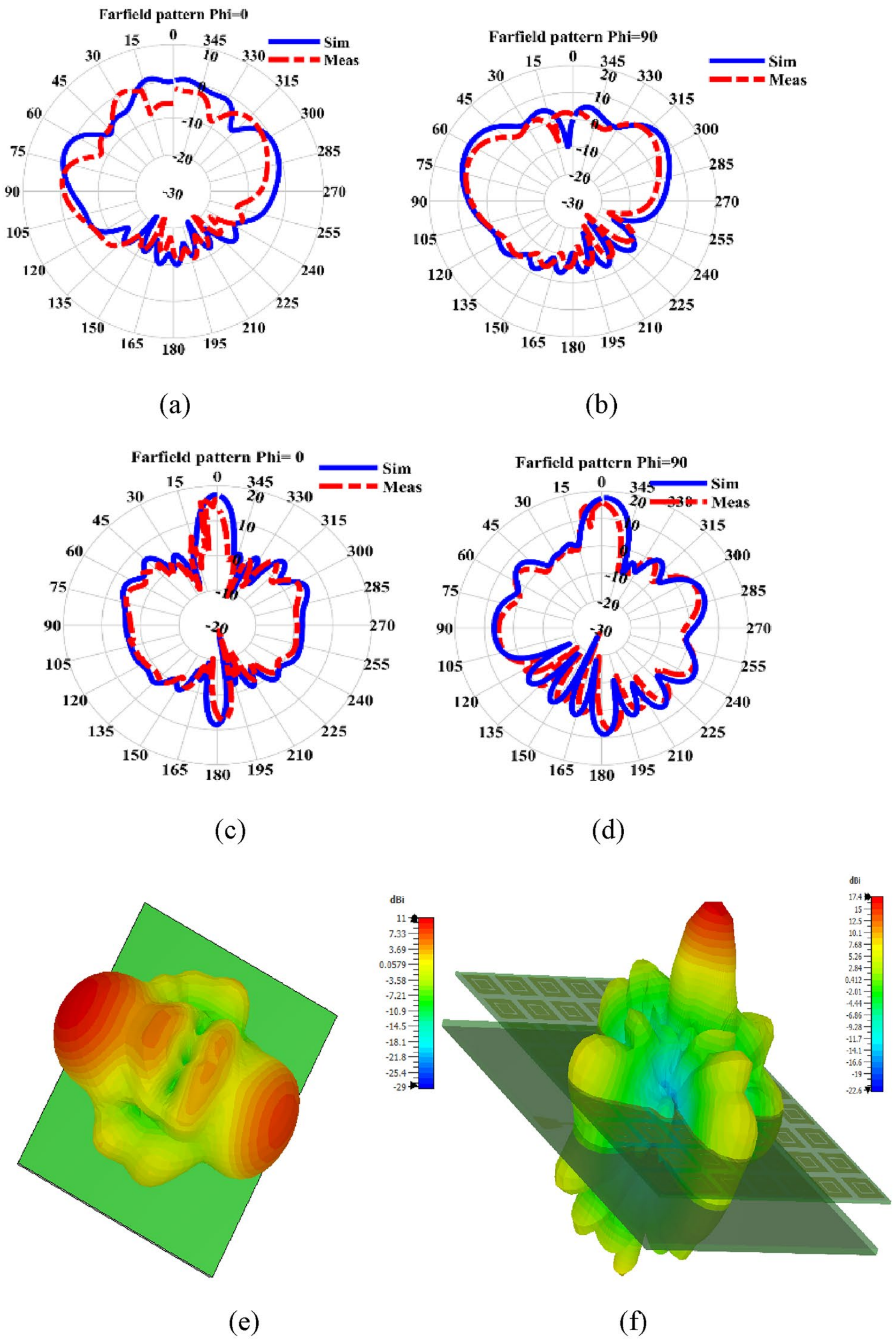

Fig. 18. Far-field radiation pattern of the feeder antenna (**a-b**), and FP antenna at 5.9 GHz in the E and H planes in (**c-d**), and 3D pattern of the final design in (**e–f**).

Parameter	Value
P_t	21, 24, 27, and 30 dBm
G_t	17.6 dBc
G_r	17.6 dBc
F	5900 MHz

Table 2. The values of different parameters used.

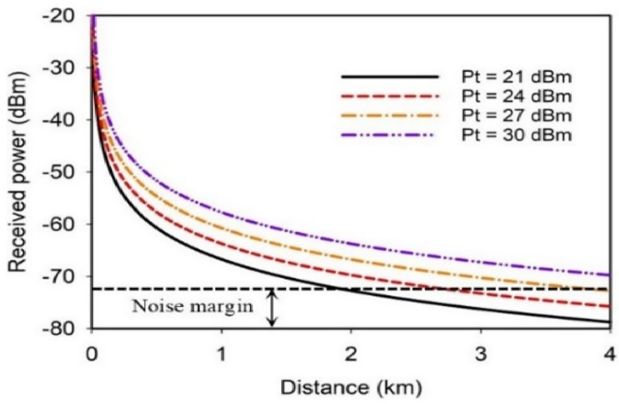

Fig. 19. Link margin of the proposed design.

a good fit for V2V and V2I communications in onboard units (OBUs). In contrast, the FP antenna with the PRS layer (depicted in Figs. 18(c-d)) demonstrates directional behavior with high gain, making it ideal for integration into roadside units (RSUs) to ensure reliable Infrastructure-to-Vehicle (I2V) communication. Figs 18 (e–f) obtained from CST Microwave Studio (suite), shows that adding the PRS layer enhances the gain and makes the radiation pattern more directional[46].

To sum up, the proposed antenna effectively fulfills its primary design objectives for vehicular communication by integrating a Sierpinski fractal array with a dual-layer PRS-based FPC. The antenna achieves a measured peak gain of 17.72 dBc, significantly higher than the 7 dBc gain of the base fractal array, demonstrating the effectiveness of PRS integration in enhancing radiation performance. It maintains an AR below 3 dB across a 490 MHz bandwidth, ensuring stable circular polarization, which is critical for V2V and V2I applications where signal alignment can vary due to dynamic vehicle movement. In comparison to recent works such as[47,48], which report gains of 13–15 dBc using more complex multilayer structures, the proposed design delivers superior gain and broader bandwidth with a simpler, low-profile configuration. The use of fractal geometry contributes to size reduction and introduces multi-resonant behavior, enhancing the design's suitability for space-constrained automotive environments. Full-wave simulations and experimental measurements consistently validate the antenna's performance and practicality, positioning it as a strong candidate for modern V2X systems where high gain, polarization stability, and ease of integration are essential.

Link budget of the proposed antenna

To verify the effective communication range of the proposed antenna, a link budget analysis was performed at 5.9 GHz. The link margin calculations were performed while considering all the gains and losses that a transmitting signal experiences while propagating through the medium. The link margin was evaluated based on the well-known equations given in[55]. The values of different parameters used are given in Table 2. The noise margin or receiver sensitivity was evaluated based on (21)[45]:

$$\mathrm{MDS} = 10\log_{10}\left(\frac{\mathrm{kT}}{1\mathrm{mW}}\right) + \mathrm{NoiseFigure} + 10\log_{10}\left(\mathrm{Bandwidth}\right) \tag{19}$$

Where MDS (minimum detectable signal) is calculated using the formula involving temperature T (290 K) and Boltzmann's constant k (−228 dBW/(kHz)). For a bandwidth of MHz and a noise figure of 13.87 dB, the calculated MDS for the proposed antenna is −72 dBm. The link margin is evaluated for various transmitted power levels (P_t = 21, 24, 27 and 30 dBm), as shown in Fig. 19. It shows that the proposed antenna can maintain a stable communication link up to a minimum distance of 1.9 km for P_t = 21 dBm and up to 4 km for P_t = 30 dBm making it a suitable candidate for various IoT and vehicular communication applications.

Application of the proposed design

Figs 20 (a-d) shows the effectiveness of the proposed design in ITS. The proposed design is positioned on top of the smart car. This simulation is performed in CST Microwave Studio (Suite)[46]. To avoid direct contact, a

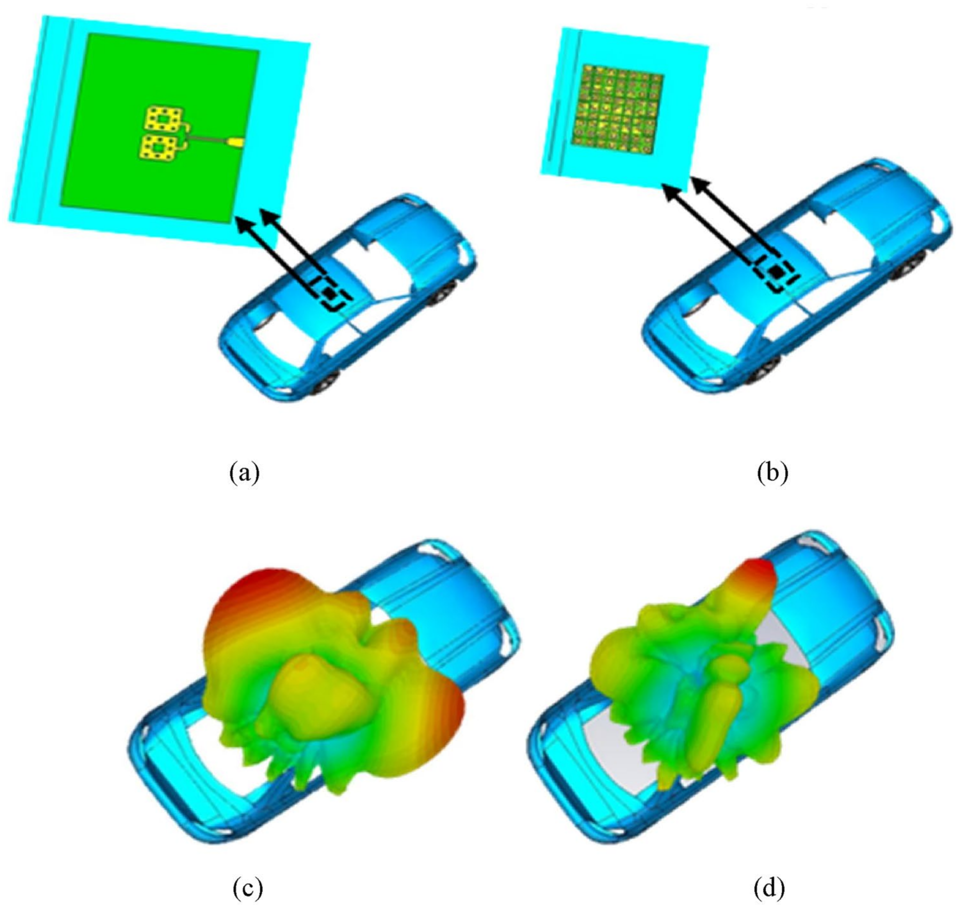

Fig. 20. (**a-d**): Simulation of the proposed design on ITS. (**a**) proposed design without PRS on ITS, (**b**) proposed design with PRS on ITS, (**c**) far-field pattern of the proposed design without PRS, and (**d**) far-field pattern of the proposed design with PRS.

gap of 15 mm is maintained between the conducting part of the car and the ground of the radiating element. Initially, the design without PRS is simulated on the car, showing exactly the same behavior as is shown by the simulated design alone. This performance of the simulated design without PRS shows its effectiveness for V2V communication. The second scenario is to simulate the PRS-based FP antenna on the car roof while considering the same conditions. The simulation shows again a similar performance, showing its effectiveness for the V2I applications.

Importantly, weather conditions and dense urban infrastructure may cause signal degradation and multipath propagation due to reflection from multiple sources. Similarly, high concentration of cars may cause channel congestion. These factors highly reduce the communication range, increase latency, and cause high-energy consumption. To overcome these challenges, adding diversity or MIMO characteristics to the proposed work would be a better option. As the design is already an array arrangement with PRS, which has highly increased the gain of the design, however MIMO arrangement will reduce the multipath loss and reliability issues. Weather-resistant antenna enclosures and deicing will also provide some protection to the antenna design.

Comparison with state-of-the-art

To highlight the features of the proposed antenna more effectively, a comparison of the given antenna design with the recently published works is provided in Table 3. The comparison is based on the overall compactness, achieved gain, CP feature, and number of superstrate layers. In[47], the design has low gain and a complex structure. Moreover, the design does not cover the operating band required for vehicular communication. In[48], the design has a two-layer complex structure with low gain and an operating band other than required for vehicular communication. Similarly[49,50], and [51] have low gain and bulky size without focusing vehicular communication band. Research works in[52] and [53] are two-layer complex structures with the gain values very less than the vehicular communication requirement. Research in[54] is bulky with no CP feature, which makes the reception of the signal difficult in a vehicular communication environment. In[55], the design is compact, simple in structure, with a CP feature. Unfortunately, the design gain does not meet the target wireless application requirement. In[56] and [57], the designs are multi-layer layers thus adding to the design complexity and increasing overall volume. Thus, multiple research problems make these designs ineffective for the target wireless application. Interestingly, the proposed design has outperformed the published designs by attaining compactness without design complexity, high gain,

Refernce	Antenna type	Operating bandwidth (GHz)	LP/CP	Max Gain	size (λ_0^3)	No. of substrate layers
Proposed work	FPC	5.47–6.1	CP	17.72 dBc	2.8 × 2.7 × 0.38	1
[47]	FPC	11.32—17.35	-	14.72	1.72 × 1.96 × 0.62	1
[48]	FPC	3.82–6.01	-	14.5	2 × 2 × 0.88	2
[49]	FPC	23.5—28.2	-	14.2	3.473.47 × 0.68	2
[50]	FPC	7.99–9.02	CP	16.83 dBc	2.13 × 2.13 × 0.56	2
[51]	FPC & AMC	9–9.9	CP	19.8 dBc	2.85 × 2.85 × 0.54	3
[52]	FPC	8.3 to 11.25	-	10.35	2.41 × 2.41 × 0.63	2
[53]	FPC	5.01–5.96	CP	11.73 dBc	1 × 1 × 0.5	2
[54]	FPC	4.0–9.0	-	14.6	3.2 × 3.2 × 0.57	1
[55]	FPC	4.5–7.5	CP	12.82 dBc	1.5 × 1.5 × 0.5	1
[56]	FPC	9.4–9.5, 10.4–10.5	-	16.2	5.1 × 5.1 × 1.03	Multi
[57]	FPC	11.5–15.2	CP		2 × 2 × 0.47	Multi
[58]	FPC	2.5	-	< 9	0.96 × 0.96 × 0.07	1
[59]	FPC	24–34.1	CP	11 dBc	1.1 × 1.1 × 0.093	1
[60]	Metasurface	23.9–30.7	CP	9.4 dBc	1.65 × 1.65 × 0.043 at 25 GHz	1
[61]	Metasurface	1.575	-	5.9	0.45 × 0.36 × 0.08	2
[62]	Metasurface	3	-	12	1.2 × 1.2 × 0.015	1

Table 3. Comparison of the proposed design with the recently published works.

and wideband with a CP feature while incorporating a single PRS layer. The proposed antenna exhibits excellent radiation performance, validating the accuracy and effectiveness of the design.

Conclusion

Data availability
The data used and/or analyzed during the current study may be available from the corresponding author upon reasonable request under applicable policies.

Received: 29 March 2025; Accepted: 15 April 2026
Published online: 07 May 2026

References
1. Cidronali, A., Maddio, S., Passafiume, M. & Manes, G. Car talk: Technologies for vehicle-to-roadside communications. *IEEE Microw. Mag.* **17**, 40–60 (2016).
2. Winkler, C. et al. Investigation of antennas for car-to-car communications. In *2020 Int. Appl. Comput. Electromagn. Soc. Symp. (ACES)* 1-2 (2020).
3. Miao, Z. et al. A tri-band circularly polarized shared-aperture patch/Fabry–Pérot antenna for satellite communication. *IEEE Antennas Wirel. Propag. Lett.* **23**, 4423–4427 (2024).
4. Dhanaraj, P. & Maheswari, S. U. Performance analysis of electrically coupled SRR bowtie antenna for wireless broadband communications. *Wirel. Netw.* **26**, 5271–5283 (2020).
5. Hosseini, A., Capolino, F. & De Flaviis, F. Gain enhancement of a V-band antenna using a Fabry-Pérot cavity with a self-sustained all-metal cap with FSS. *IEEE Trans. Antennas Propag.* **63**, 909–921 (2015).
6. Niaz, M. J. et al. Wideband Fabry-Perot resonator antenna employing a multilayer partially reflective surface. *IEEE Trans. Antennas Propag.* **69**, 2404–2409 (2021).
7. Zhang, Y., Li, Y., Hu, M., Wu, P. & Wang, H. Dual-band circular-polarized microstrip antenna for ultrawideband positioning in smartphones with flexible liquid crystal polymer process. *IEEE Trans. Antennas Propag.* **71**(4), 3155–3163. https://doi.org/10.1109/TAP.2023.3247130 (2023).
8. Hu, M., Li, Y., Zhang, Y., Wu, P. & Wang, H. Ultrathin dual-band circularly polarized antenna. *IEEE Antennas Wirel. Propag. Lett.* **23**(3), 930–934. https://doi.org/10.1109/LAWP.2023.3339203 (2024).
9. Zhang, Z., Li, K., Chen, D. & Z., Z. Y. Z. Y. An optically transparent near-zero-index grating metamaterial for enhanced on-glass millimeter-wave radiation. *IEEE Trans. Antennas Propag.* **73**(6), 4092–4097. https://doi.org/10.1109/TAP.2025.3543073 (2025).
10. Zhang, Y., Li, Y., Zhang, W., Zhang, Z. & Feng, Z. Omnidirectional antenna diversity system for high-speed onboard communication. *Engineering* **11**(4), 72–79 (2022).
11. Zhang, Y., Liu, P., Yin, Y. & Li, Y. Omnidirectional dual-polarized antenna using colocated slots with wedgy profile. *IEEE Trans. Antennas Propag.* **69**(9), 5446–5454. https://doi.org/10.1109/TAP.2021.3069517 (2021).
12. Zhang, Y. & Li, Y. Scalable omnidirectional dual-polarized antenna using cavity and slot-dipole hybrid structure. *IEEE Trans. Antennas Propag.* **70**(6), 4215–4223. https://doi.org/10.1109/TAP.2021.3138552 (2022).
13. Zhao, X. et al. A high-gain Fabry-Perot resonator antenna with dual-sense circular polarization diversity. *IEEE Antennas Wirel. Propag. Lett.* **23**, 1–5 (2024).
14. Burokur, S.N. et al. Metamaterials and metasurfaces for industrial antenna applications. *Parisnanterre.fr* (2018).
15. Ziolkowski, R. W. Metamaterials and antennas. In *Handb. Antenna Technol.* 287–320 (2016).
16. Krzysztofik,W.J. Fractals in antennas and metamaterials applications *Fractal Anal. Appl. Phys. Eng. Technol.* (2017).
17. Arora, C., Pattnaik, S. S. & Baral, R. N. Metamaterial inspired DNG superstrate for performance improvement of microstrip patch antenna array. *Int. J. Microw. Wireless. Technol.* **10**, 318–327 (2018).
18. Enoch, S. et al. A metamaterial for directive emission. *Phys. Rev. Lett.* https://doi.org/10.1103/PhysRevLett.89.213902 (2002).
19. Li, A., Singh, S. & Sievenpiper, D. Metasurfaces and their applications. *Nanophotonics* **7**, 989–1011 (2018).

20. Dey, S. & Dey, S. Broadband high-gain cavity resonator antenna using planar electromagnetic bandgap (EBG) superstrate. *Int. J. Microw. Wirel. Technol.* **15**, 90–101 (2022).
21. El Yassini, A. et al. Design of circular patch antenna with a high gain by using a novel artificial planar dual-layer metamaterial superstrate. *Int. J. RF Microw. Comput. Aided Eng.* **29**(11), e21939 (2019).
22. Razi, Z. M., Rezaei, P. & Valizade, A. A novel design of Fabry-Perot antenna using metamaterial superstrate for gain and bandwidth enhancement. *AEU* **69**, 1525–1532 (2015).
23. Lima, A. M., Cunha, N. H. O., Silva, J. P. & Da.,. Effect of metamaterial cell array on a microstrip patch antenna design. *J. Microw. Optoelectron. Electromagn. Appl.* **19**(327), 342 (2020).
24. Kim, H. et al. Design and implementation of electromagnetic band-gap embedded antenna for vehicle-to-everything communications in vehicular systems. *ETRI J.* **41**, 731–738 (2019).
25. Lv, Y.-H., Ding, X. & Wang, B. Dual-wideband high-gain Fabry-Perot cavity antenna. *IEEE Access* **8**, 4754–4760 (2020).
26. Zhu, L. et al. A broadband Fabry–Perot resonator antenna using a partially reflecting surface with positive reflection phase gradient. *AIP Adv.* https://doi.org/10.1063/5.0103604 (2022).
27. Sheng, X. et al. Design of broadband high-gain Fabry-Pérot antenna using frequency-selective surface. *Sensors* **22**, 9698 (2022).
28. Fang, S. et al. A wideband Fabry-Perot cavity antenna with single-layer partially reflective surface. *IEEE Antennas Wirel. Propag. Lett.* **22**, 412–416 (2023).
29. Akkole, S., Vasudevan,N. Compact multiband microstrip fractal antenna design for wireless applications – an overview. In *4th Int. Conf. Electron. Commun. Aerosp. Technol. (ICECA)* 554–558 (2020).
30. Almizan, H. et al. Novel metasurface-based microstrip antenna design for gain enhancement. RF harvesting. *Infocommun. J.* **15**, 2–8 (2023).
31. Al-Rawe, A. et al. A dual-band high efficiency fractal rectenna for RF energy harvesting systems. In *2023 5th Int. Congr. Hum. Comput. Interact. Optim. Robot. Appl. (HORA)* 1–4 (2023).
32. Almizan, H., Elwi, T. A. & Hassain, A. Circularly-polarized, wide-range coverage azimuth and elevation angles microstrip antenna for RF harvesting. *J. Eng. Sustain. Dev.* **24**, 191–198 (2020).
33. Ghadeer, S.H. et al. Ultra-wideband MIMO antenna array for mm-wave 5G applications. In *2023 IEEE Int. Symp. Antennas Propag. (ISAP)* 1–2 (2023).
34. Al-Saegh, A. M. et al. AI-based investigation and mitigation of rain effect on channel performance with the aid of a novel 3D slot array antenna design for high high-throughput satellite system. *IEEE Access* **12**, 29926–29939 (2024).
35. Elwi, T. A. et al. On the performance of a photonic reconfigurable electromagnetic band gap antenna array for 5G applications. *IEEE Access* **12**, 60849–60862 (2024).
36. Rasheed, W.S. et al. Reconfigurable microstrip antenna design for fifth generation (5G) system. In *2024 Int. Conf. Distrib. Comput. Optim. Tech. (ICDCOT)*, 1–6 (2024).
37. Zhang, J. & Wong, H. A high-gain millimeter-wave Fabry-Perot cavity antenna with phase correction on a meta-ground reflective surface. *IEEE Trans. Antennas Propag.* **72**, 6187–6194 (2024).
38. Hussein, H. et al. A novel MIMO antenna integrated with a solar panel and employing AI-equalization for 5G wireless communication networks. *IEEE Access* **12**, 114382–114393 (2024).
39. Jwair, M. H. et al. Intelligent metasurface layer for direct antenna amplitude modulation scheme. *IEEE Access* **11**, 77506–77517 (2023).
40. Yehia, S. et al. Design of compact flexible UWB antenna using different substrate materials for WBAN applications. In *2022 Photonics Electromagn. Res. Symp. (PIERS)*, 373–378 (2023).
41. Yehia, S et al. Flexible antenna design for wearable telemedicine applications. In *Photon. Electromagn. Res. Symp. (PIERS)* (2023).
42. Ez-Zaki, F., Ghammaz, A. & Belahrach, H. Performance improvement of corner-truncated Sierpinski carpet fractal antenna using U-tree slots for vehicular communications and other bands. *Lect. Notes Netw. Syst.*, 1091–1100 (2021).
43. Gurjar, R. et al. A compact modified Sierpinski carpet fractal UWB MIMO antenna with square-shaped funnel-like ground stub. *AEU Int. J. Electron. Commun.* **117**, 153126 (2020).
44. Slimani, A. et al. Gain and bandwidth enhancement of new planar microstrip array antennas geometry for C band weather radar applications. *Int. J. Microw. Wirel. Technol.* **9**, 1139–1146 (2016).
45. Narayan, S. & Kesavan, A. *Handbook of Metamaterial-Derived Frequency Selective Surfaces* (Springer Nature, 2023).
46. https://www.3ds.com/products/simulia/cst-studio-suite/workflow-integration.
47. Chen, Q. et al. Cross-shaped interconnected receiver–transmitter metasurface for a circularly polarized Fabry-Pérot antenna. *IEEE Access* **10**, 112019–112027 (2022).
48. Wang, Y. & Zhang, A. Dual circularly polarized Fabry-Perot resonator antenna employing a polarization conversion metasurface. *IEEE Access* **9**, 44881–44887 (2021).
49. An, K., Sun, P. & Chen, A. A high gain and high radiation efficiency optical transparent Fabry-Perot cavity antenna. *Electron. Lett.* **60**(8), e13203 (2024).
50. De, R., Abegaonkar, M. P. & Basu, A. A. broadband circularly polarized Fabry Perot antenna with spatially separated superstrate area excitation for CubeSat applications. *Sci. Rep.* **13**(1), 11224 (2023).
51. Melouki, N., Hocini, A. & Denidni, T. A. High-gain and wideband Fabry-Perot resonator antenna based on a compact single PRS layer. *IEEE Access* **10**, 96526–96537 (2022).
52. Liu, Z.-G. & Lu, W.-B. Low-profile design of broadband high-gain circularly polarized Fabry-Perot resonator antenna and its array with linearly polarized feed. *IEEE Access* **5**, 7164–7172 (2017).
53. Budarapu, S. K. et al. Performance enhancement of patch antenna using RIS and metamaterial superstrate for wireless applications. *Prog. Electromagn. Res. C* **130**, 95–105 (2023).
54. Le-Huu, T. et al. A high-gain filtering Fabry-Perot antenna with RCS reduction. *IEEE Access* **11**, 145723–145731 (2023).
55. Supreeyatitikul, N., Boonpoonga, A. & Phongcharoenpanich, C. Z-shaped metasurface-based wideband circularly polarized Fabry-Pérot antenna for C-band satellite technology. *IEEE Access* **10**, 59428–59441 (2022).
56. Huang, J. W. et al. Design of a high-gain duplex antenna with multibeam radiation based on a Fabry-Pérot cavity.. *IEEE Trans. Veh. Technol.* https://doi.org/10.1109/TVT.2025.3541196 (2025).
57. Deng, X. et al. Axial ratio bandwidth enhancement of DBDCP Fabry-Pérot cavity antenna for vehicular MIMO communications and sensing. *IEEE Trans. Veh. Technol.* **73**, 3421–3429 (2023).
58. Hongnara, T., Chaimool, S., Akkaraekthalin, P. & Zhao, Y. Design of compact beam-steering antennas using a metasurface formed by uniform square rings. *IEEE Access* **6**, 9420–9429 (2018).
59. Hussain, N., Jeong, M.-J., Abbas, A., Kim, T.-J. & Kim, N. A metasurface-based low-profile wideband circularly polarized patch antenna for 5G millimeter-wave systems. *IEEE Access* **8**, 22127–22135. https://doi.org/10.1109/ACCESS.2020.2969964 (2020).
60. Cao, T. N. et al. Millimeter-wave broadband MIMO antenna using metasurfaces for 5G cellular networks. *Int. J. RF Microw. Comput. Aided Eng.* **2023**, 1–11. https://doi.org/10.1155/2023/9938824 (2023).
61. Sundas Farooq Bilal MuhammadTariq Mairaj Rasool, K. K. K. Low profile high gain RHCP antenna for L-Band and S-Band using rectangular ring metasurface with backlobe suppression. *PLoS One* **19**(2), e0297957 (2024).
62. Badawe, M. E., Almoneef, T. S. & Ramahi, O. M. *A true metasurface antena. Sci. Rep.* **6**, 1–8. https://doi.org/10.1038/srep19268 (2016).

Acknowledgements
This work is partially supported by the National Science Centre of Poland Grant 2020/37/B/ST7/01448 and 2022/47/B/ST7/00072 and by the Icelandic Research Fund Grant 2410297.

Author contributions
" Conceptualization, Sh. K and O.O and H.B, and A.G and S.U; methodology, S.K and J.N and F.E and Sl. K and Sh. K and S.U and L.M; formal analysis, F.E. and Sh. K and Sl. K and L.M; data management, Sh.K.; writing original draft, F.E. and Sl. K and J.N.; project administration, O.O. and A.G, and S.K and L.M; funding acquisition, Sh. K and J.N. and M.K, and Sl.K. All authors have read and agreed to the published version of the manuscript."

Funding
National Science Center of Poland,2022/47/B/ST7/00072,2020/37/B/ST7/01448,Icelandic Research Fund Grant,2410297

Declarations

Competing interests
The authors declare no competing interests.

Additional information
Supplementary Information The online version contains supplementary material available at https://doi.org/10.1038/s41598-026-49516-w.

Correspondence and requests for materials should be addressed to L.M.